Title: Label free, capillary-scale blood flow mapping *in vivo* reveals that low intensity focused ultrasound evokes persistent dilation in cortical microvasculature

YuBing Shen[1], Jyoti V. Jethe[1], Jacob Hehir[1], Marcello Magri Amaral[2,3], Chao Ren[4], Senyue Hao[5], Chao Zhou[2,4,5], and Jonathan A. N. Fisher[1]*

[1] *Department of Physiology, New York Medical College, Valhalla, NY, USA*
[2] *Department of Biomedical Engineering, Washington University in St Louis, St. Louis, MO, USA*
[3] *Biomedical Engineering, Universidade Brasil, San Paulo, SP, Brazil*
[4] *Imaging Science Ph.D. Program, Washington University in St Louis, St. Louis, MO, USA*
[5] *Department of Electrical & Systems Engineering, Washington University in St Louis, St. Louis, MO, USA*

* *correspondence to fisherworks@gmail.com*

Abstract

Non-invasive, low intensity focused ultrasound (FUS) is an emerging neuromodulation technique that offers the potential for precision, personalized therapy. An increasing body of research has identified mechanosensitive ion channels that can be modulated by FUS and support acute electrical activity in neurons. However, neuromodulatory effects that persist from hours to days have also been reported. The brain's ability to provide targeted blood flow to electrically active regions involve a multitude of non-neuronal cell types and signaling pathways in the cerebral vasculature; an open question is whether persistent effects can be attributed, at least partly, to vascular mechanisms. Using a novel *in vivo* optical approach, we found that microvascular responses, unlike larger vessels which prior investigations have explored, exhibit persistent dilation. This finding and approach offers a heretofore unseen aspect of the effects of FUS *in vivo* and indicate that concurrent changes in neurovascular function may partially underly persistent neuromodulatory effects.

Introduction

Low-intensity focused ultrasound (FUS) is an emerging technology for non-invasive neuromodulation. Compared with other non-invasive modalities such as transcranial magnetic stimulation (TMS) or transcranial direct current stimulation (tDCS), FUS offers the potential for restricting modulatory stimuli to within volumes that are ~3-5 orders of magnitude smaller and with millimeter-scale cross-sectional focal area (Tufail et al., 2011; Yoo et al., 2011a; Deng et al., 2013; Rampersad et al., 2014; Kubanek, 2018). These resolution advantages offer the possibility for minimizing off-target effects as well as the potential for more precise, personalized treatment. In human subjects, FUS has been explored as a therapeutic for a wide range of conditions such as stroke (Yüksel et al., 2023), Alzheimer's disease (Leinenga and Götz, 2015; Lin et al., 2015), essential tremor (Rohani and Fasano, 2017; Sharabi et al., 2019), Parkinson's disease (Lee et al., 2022; Zhong et al., 2023), as well as chronic pain (Hameroff et al., 2013). Beyond therapy, FUS has been shown to acutely modify sensory evoked neural responses in small animal models (Kim et al., 2014), swine (Dallapiazza et al., 2018), nonhuman primates (Folloni et al., 2019), and humans (Ai et al., 2018). Given that FUS has the capability of evoking sensations including somatosensory (Legon et al., 2014, 2018; Lee et al., 2015, 2016; Kim et al., 2023) and visual (Deffieux et al., 2013; Lu et al., 2021), this modality has presented new stimulus methods for brain-computer-interface applications (Yoo et al., 2013; Lee et al., 2017; Kosnoff et al., 2023).

Central to wider clinical adoption is a clearer understanding of dosage and effects. The parameter space for designing stimuli and dosing is wide, and altering individual parameters such as duty cycle has been found to qualitatively change the effects on the brain and their associated timescales (King et al., 2013). For example, in some instances, altering duty cycle was found to shift effects from excitatory to inhibitory even when the average pressure is not changed (Plaksin et al., 2016).

Recent work on mechanisms has provided compelling evidence that FUS elicits action potentials in neurons by activating mechanosensitive Ca^{2+} channels that include TRPP1, TRPP2, TRPC1, and Piezo1 (Yoo et al., 2022). FUS stimulation has also been shown to increase Ca^{2+} influx in astrocytes by opening TRPA1 channels, resulting in glutamate release through Bestrophin-1 (Best1) channels (Oh et al., 2019).

Beyond acute electrophysiological effects, FUS can elicit persistent plasticity (Yoo et al., 2011a, 2018; Folloni et al., 2019) up to weeks, in some studies (Niu et al., 2022; Zhao et al., 2023). In terms of underlying mechanisms for these chronic effects, FUS appears to modulate the function of NMDA receptors (Darmani et al., 2022), a key contributor to many forms of synaptic plasticity (Dudek and Bear, 1992; Bliss and Collingridge, 1993; Feldman, 2009). Zhao et al. (2023) suggested that FUS-induced increases in expression of brain-derived neurotrophic factor (BDNF), glial cell line-derived neurotrophic factor (GDNF), and vascular endothelial growth factor (VEGF) could underly the increased growth rate of dendritic spines that they observed over a 28-day course of repeated doses of FUS (Lin et al., 2015; Huang et al., 2017).

Sonication-evoked cerebrovascular effects and hemodynamics, generally considered secondary to neuronal activity (Phillips et al., 2016), could also underly at least some of the observed neuromodulatory effects. Neuronal activity elicits cerebral blood flow and cerebral blood volume changes that are spatially restricted to roughly the same areas that are electrically active. This phenomenon, termed neurovascular coupling, is the result of an intricate choreography of multiple cell types and signaling mechanisms (Iadecola, 2017) and perturbing vasculature would impact neuronal function. In terms of potential mechanisms, some of the same mechanosensitive channels found to be critical for FUS-induced neural effects are also expressed in vasculature. TRPC1, for example, is expressed in vascular endothelial cells (TIRUPPATHI et al., 2006; Ma et al., 2011;

Earley and Brayden, 2015), TRPP1 in vascular smooth muscle cells (Griffin et al., 1997; Torres et al., 2001; Narayanan et al., 2013), and Piezo1 is expressed in both cell types and also plays a critical role in vascular development and remodeling (Ranade et al., 2014; Retailleau et al., 2015; Harraz et al., 2021). Because hemodynamic responses lag neural activation, vascular effects could potentially contribute to persistent apparent neuroplasticity.

The impact of FUS on cerebral hemodynamics has been studied using invasive and noninvasive methods. Functional magnetic resonance imaging (fMRI), for example, has been instrumental in noninvasively exploring the deep brain effects of FUS neuromodulation as well as its viability in larger brains including humans. fMRI has revealed FUS-induced hyperaemia both cortically and subcortically by means of volumetric blood-oxygen-level-dependent (BOLD) signals (Folloni et al., 2019; Kim et al., 2023). Near infrared spectroscopy (NIRS) (Strangman et al., 2002a), another non-invasive approach for monitoring cerebral hemodynamics, has been used to measure hemodynamic signals evoked by administering FUS to the somatosensory cortex (Kim et al., 2019). While generally lacking the spatial resolution of fMRI, NIRS can monitor hemodynamics with much higher temporal resolution (Strangman et al., 2002b). Kim et al. found that the FUS-induced hemodynamic response, measured in terms of inferred changes in oxy- and deoxyhemoglobin concentrations, largely resolves within 20 seconds. That timescale is similar to sensory-evoked hyperaemia measured using NIRS (Ferrari and Quaresima, 2012). Unlike noninvasive measurements, which have relatively coarse spatial resolution, invasive imaging techniques such as laser speckle contrast imaging (Yuan et al., 2018, 2020) and optical intrinsic signal imaging (OISI; Yuan et al., 2023) have resolved FUS-induced flow changes and dilation in individual vessels. Mirroring the NIRS findings, these studies have similarly observed FUS-induced hemodynamic responses in individual vessels largely subside within ~15 seconds.

While the results of FUS-associated hemodynamic measurements seemingly suggest that acute effects are likely of neuronal or astrocytic origin and that persistent neuromodulatory effects do not manifest in prolonged vasomodulation, none of these experiments has heretofore directly resolved the impact of FUS alone on microvasculature. For widefield optical techniques such as laser speckle and OISI, this is partly owing to relatively poor axial resolution due to the use of low numerical aperture lenses. Measuring the functional response in small vessels is critical because microvascular branches ~3−15 μm in diameter, which include capillaries, small arterioles, and venules, are at the frontline for neurovascular coupling (Iadecola, 2017; Sweeney et al., 2018) and also likely easier to perturb mechanically by FUS (Cho et al., 2011).

To obtain insight into a potential microvascular reflection of persistent effects following sonication, we developed a label-free optical approach for interrogating blood flow in vasculature down to capillary scale *in vivo* directly at the site of ultrasound delivery. Our apparatus used a custom spectral domain optical coherence tomography angiography (OCT-A) device that measures blood flow based on scattering changes in moving red blood cells. Compared with other optical modalities for measuring blood flow at microvascular scales, OCT-A offers the advantage of being label free, in contrast with other optical techniques such as two-photon microscopy, which requires intravenous tracers or targeted expression of fluorescent reporters. Additionally, because the depth resolution in OCT is limited by the characteristics of the broadband light source rather than an objective's optical depth of field (Aumann et al., 2019), relatively low-numerical aperture, long working distance lenses can be used to survey large brain regions without sacrificing depth resolution. Integrating this with a wide-aperture ring transducer whose acoustic and optical foci were co-localized, we were able to obtain a direct glance into the effects of FUS on cortical microvasculature.

Results

In situ, label-free microvascular-level blood flow measurements during FUS neuromodulation

Using a custom spectral domain OCT-A apparatus (Fig. 1A) that was able to compensate for long working distances that traversed ~10 cm of water within the ring transducer, we were able to obtain 3D portraits of vasculature (Fig. 1B) with 2.48 × 3.48 μm (axial × lateral) resolution at depths upwards of 650 μm, label free in wild-type mice. Whereas techniques such as MR-acoustic radiation force imaging (MR-ARFI) can be used to localize the FUS focus in fMRI experiments (McDannold and Maier, 2008), a challenge for targeting FUS in epi-illumination optical systems *in vivo* is that the FUS beam is not intrinsically optically detectable. Because small positioning errors can lead to uneven sonication patterns within an optical field of view, we used a phased array ring transducer with a beam width larger than the analyzed zones (Fig. 1C) to ensure that our analysis was restricted to vessels that received the same FUS dosing.

Compared with vascular analysis and tabulation based on two-photon imaging (Blinder et al., 2013), the vessel morphology is of lower signal-to-noise. We therefore developed an image processing pipeline that was able to selectively segment vessel branches based on diameter, thereby permitting us to selectively analyze flow and dilation dynamics in diverse vessel populations. Figs. 2 and 3 demonstrate that OCT-A signals can be selectively analyzed over narrow depth ranges to reveal depth-dependent flow components. Figs. 2A and B, for example show z-projections taken over narrow, ~2-μm ranges centered at the cortical surface and ~340 μm below. As illustrated in Fig. 2B, deeper vascular components are largely microvascular. The histogram depicted in Fig 2C reveals that vessel branches within the subregion of somatosensory cortex that

we visualized were largely of diameters below 30 μm, and vessel branches of diameters less than 10 μm accounted for ~ 48% of the total identified and tagged for analysis. A color-coded depiction of the full depth span of angiography data is shown in Fig. 2D. Fig. 3 illustrates selective segmentation of vessels by diameter, as well as our approach for both large and small vessel diameter analysis. Microvascular branches, which were detectable across all conditions, were auto-selected for analysis, as depicted in Fig. 3C, andvessel branches that could be tagged after skeletonization were tracked individually throughout the course of FUS application.

FUS elicits vascular dilation most prominently in small-diameter vessel branches

Averaged over all animals (N = 11), 510 kHz FUS (50% duty cycle, and 1 kHz pulse repetition) delivered at intensities of 1 and 10 W/cm^2 spatial-peak pulse-average intensity (I_{sppa}), for 20 seconds elicited dilation that was significant for the population of vessels of diameter less than 15 μm, but not for populations of larger diameter vessels (Fig. 4 & Table 1). Prior to FUS, the average diameter of the small vessel population was 5.9 ± 1.5 μm (mean ± standard deviation); within 10 seconds following 1 W/cm^2 (I_{sppa}) sonication, this vessel population exhibited an 18.1% ± 4.1% increase in diameter (p = 0.0009, using a two-tailed paired Student's t-test). Sonicating at a higher intensity (10 W/cm^2) yet with the same duty cycle yielded a dilation of 31.0% ±7.9% (p = 0.0016). At both intensities, dilation in small vessels following an initial sonication persisted beyond 10 minutes. In animals sonicated with the higher intensity, vessels < 15 μm in diameter exhibited a small yet significant amount of further dilation 10 minutes following sonication (33.5% ± 10.2%, p = 0.03). Otherwise, a second dose of sonication did not appear to dilate vessels significantly further (Fig. S1).

As depicted in Fig. 4A &B, larger vessel populations on average exhibited only small and mostly non-significant changes after sonication. In fact, vessels of diameter > 20 μm appeared to display a modest constriction (by 3.3% ± 3.4%), though the change was not statistically significant within our sample size (p = 0.12). Vessel segmentation and analysis at the microvascular level also enabled us to catalog and track individual vessel branches; Fig. 4D follows the dilation of one tracked sample vessel following sonication. In sham experiments, vessels of all diameter ranges did not exhibit significant changes at any time point (Table 1).

Impact of FUS on vascular permeability and tissue integrity

At high intensities, FUS can permeabilize the blood-brain barrier (BBB) and impact neurovascular response (Todd et al., 2019). To address the possibility that the vascular responses we observed were due to tissue damage or extravasation, we assessed vessel morphology and leakage of intravenously-injected Evans blue dye, which binds to serum albumin and does not leave the vasculature unless the BBB is permeated. We exposed mice to FUS at the intensity used in these experiments (1.2 W/cm^2) and, as a positive control for tissue damage, high intensity (200 W/cm^2), at adjacent locations on the same cortical hemisphere (Fig. 5). After 24 hours, sites exposed to high-intensity FUS displayed clear tissue damage as well as microvascular disruption, as visualized by vascular marker CD31. Regions targeted with high intensity FUS also displayed extravasation of Evans blue dye in the parenchyma. These effects extended beyond 350 μm in depth. In contrast, exposure to the low intensity used in these experiments (1.2 W/cm^2) yielded no evidence of gross tissue disruption nor Evans Blue dye leakage.

Discussion

The results we obtained fill a gap in exploration of vascular responses to FUS, which have heretofore measured either responses in larger vessels or in diffuse, bulk tissue hemodynamics. The closest relevant studies involved the use of two-photon microscopy to dissect microvascular changes following the combination of FUS and microbubbles (Raymond et al., 2007; Cho et al., 2011; Chen et al., 2022). Because microbubbles significantly amplify mechanical displacement due to volume oscillations, the underlying mechanisms in findings from that body of research are likely different. Those studies largely report vasoconstriction, though Cho et al. also observed modest vasodilation in small diameter vessel branches. The authors suggested that these effects could potentially be related to secondary effects of BBB-disruption, namely inflammatory responses (Pober and Cotran, 1990). This mechanism may not be unique to FUS; in the case of tDCS, for example, despite the fact that the modulatory stimulus is electrical current rather than mechanical perturbation, preclinical studies have revealed evidence that persistent plasticity may be similarly associated with an inflammatory vascular response due to perturbed BBB permeability (Shin et al., 2020). Although our observed vasoconstrictive trend in vessel branches larger than 20 μm in diameter were not statistically significant, that combined with vasodilation of smaller diameter vessels bears semblance to those previous results. Additionally, because individual vessels vary in their diameters along their length, particularly at branch points for larger vessels, quantification of potential vasoconstrictive effects could have been diluted given that microvessels represented the majority of identified vessels. At the same time, opposite trends—FUS-induced dilation of large vessels—have been observed using laser speckle imaging without microbubbles (Yuan et al., 2018). Previous microvascular observations may therefore indeed be of limited relevance.

Despite the absence of microbubbles and the fact that we found no evidence of Evans blue dye leakage, it is not unfathomable that mechanical perturbation could have activated an inflammatory response due to a small amount of BBB permeabilization that our immunohistochemical analysis was not able to resolve. Reports that have measured Evans blue leakage with other methods such as near-infrared whole brain imaging, however, have also observed persistent neuromodulation in the absence of BBB permeabilization evidence (Blackmore et al., 2021). This provides some supporting evidence that FUS alone, without BBB permeabilization can lead to persistent effects. To that point, it should be noted that *in vitro* results provide evidence for entirely vascular-independent components of persistent effects; Clennell et al. (2021), for example, found that FUS can induce up to 8 hours of sustained enhanced excitability in cultured cortical neurons, possibly due to dephosphorylation of select subunits of voltage-gated potassium channels (i.e. $K_v2.1$) (Clennell et al., 2023).

The fact that the dilation we observed in microvasculature was persistent and not associated with sensory activation suggests that the effect is not simply a reflection of FUS-triggered hyperaemia secondary to acute neural activation; for instance, we have previously shown that acute, sensory activation evokes increases in capillary blood flow that subside within ~10 sec (Jang et al., 2021). If our microvascular trends do indeed reflect a response to neuronal effects, they may be more likely related to the prolonged elevated excitability described by Clennell et al. (2011).

It is likely that the prolonged dilation is related to a combination of direct and indirect effects of FUS modulation of mechanosensitive channels in all key cell types in the neurovascular unit, i.e. astrocytes, endothelial cells, smooth muscle cells, pericytes, and of course neurons. As noted previously, endothelial cells and smooth muscle cells express some of the same FUS-sensitive mechanosensitive channels as in neurons, all of which have recently been found to be directly

sensitive to FUS, at least in culture (Newman et al., 2023). We would include in "indirect" effects the FUS-dependent release or effect of vasodilators such as nitric oxide (NO). This could originate from dilation in larger, smooth muscle cell-lined vessels in response to either FUS-induced increased NO release from astrocytes as described by Oh et al. (Oh et al., 2019), or else enhancement of NO synthase, as suggested by Yuan et al. (2018). At the capillary level, the increase in NO concentration could cause dilation by inducing relaxation of pericytes (Hall et al., 2014).

The use of anesthesia presents potential confounds for this and the majority of other FUS neuromodulation studies in small animals. On their own, many anesthetics alter hemodynamics and vascular function owing to a wide range of mechanisms including altered cerebral autoregulation, vasomotor reactivity, and neurovasular coupling (Slupe and Kirsch, 2018). Yoo et al. (Yoo et al., 2011b) found that FUS administered to the thalamus could alter anesthesia state, specifically for ketamine-xylazine. FUS administered to brainstem nuclei, particularly the dorsal raphe nucleus, has also been shown to accelerate recovery from isoflurane-induced anesthesia (He et al., 2023). Decades of experimental and theoretical research has shown that systems-level thalamocortical oscillations and their interplay with brainstem nuclei serve a controlling role in regulating consciousness under anesthesia (Contreras et al., 1997; White and Alkire, 2003; Llinás and Steriade, 2006; Gili et al., 2013; Guldenmund et al., 2013; Mashour and Alkire, 2013; Ching and Brown, 2014; Brown et al., 2018; Redinbaugh et al., 2020). It is unsurprising, therefore, that directing FUS subcortically to those regions affects recovery from anesthesia. In our experiments, FUS was directed laterally at the somatosensory cortex, intentionally minimizing the possibility of affecting subcortical structures. Furthermore, we maintained isoflurane concentrations below 2%, which was the level used by He et al. (He et al., 2023) It therefore is possible, albeit unlikely,

that some degree of our observations reflected FUS modulation of state of anesthesia. Nevertheless, the absence of any significant overall diameter changes in sham experiments offers evidence that the post-FUS dilation did not reflect global physiological trends that evolved during the course of the experiment.

Ultimately, the broad concept of "persistent effects" owing to FUS neuromodulation likely reflects a conglomeration of neural, astrocytic, and vascular phenomena. We observed vascular dynamics in microvasculature that unexpectedly differs significantly from the responses in larger vessels that feed into the vascular network. Taken together with the recent *in vitro* findings that pericytes are FUS-sensitive, further *in vivo* experiments will be critical to parse the various underlying mechanisms and cellular origins that lead to short and longer-term neural and behavioral effects. Future investigations using flow direction sensitive OCT-A could help distinguish arterial vs. venous flow in the cerebrovascular networks. Given differences in their role in neurovascular coupling, we would expect to find differential effects. Additionally, integrating two-photon microscopy in-line with OCT angiography (Kim et al., 2013) could permit us to individually correlate Ca^{2+} dynamics, in various cell types, with localized microvascular blood flow. A more holistic understanding of all the mechanisms of FUS neuromodulation could also increase the predictive accuracy and relevance of computational modeling. For noninvasive electromagnetic modalities such as TMS or tDCS, direct effects on electrophysiological function can be simulated using standard finite element methods (Neuling et al., 2012; Iacono et al., 2015; Saturnino et al., 2019). An equally representative capability to do so for FUS would enable more systematic, hypothesis-driven experimental design.

Methods

Surgical procedures

All animal experiments were performed in accordance with the guidelines of the institutional Animal Care and Use Committee of New York Medical College. Adult C57BL/6J mice between two to five months were anesthetized with an initial dose of 5% isoflurane (vaporized in medical grade compressed oxygen) for < 20s and was later maintained at 1.5%. Following initial anesthesia induction, animals were positioned in a stereotaxic apparatus (Stoelting Co., Wood Dale, IL) and eyes were covered with petrolatum ophthalmic ointment (Puralube®, Fera Pharmaceuticals, Locust Valley, NY). Mice were administered buprenorphine (0.5mg/kg, subcutaneously) and dexamethasone (0.2mg/kg, subcutaneously) to reduce inflammation, and body temperature was measured and maintained at 37°C with a closed-loop temperature-controlled heating system that included a heating pad (TC-1000, CWE, Ardmore, PA) and rectal probe (40-90-8D, FHC, Inc., Bowdoin, ME). Respiratory rate was monitored and maintained at ~100 breaths/min during the surgical and experimental procedures.

In preparation for the craniotomy procedure, the scalp was infused with lidocaine delivered subcutaneously and a midline incision was performed on the region overlying the forelimb's representation on the primary somatosensory cortex (at the same point on the rostrocaudal axis as bregma and ~2.5 mm lateral).

A custom-fabricated aluminum headbar was affixed to the left side of the exposed skull with cyanoacrylate adhesive (Loctite 454, HenKel, Wisconsin) to improve positioning for surgical and experimental procedures. A 2.5 × 3 mm rectangular craniotomy was made using a handheld dental drill (Osada Model EXL-M40), being careful not to damage the dura mater. To maximize

combined optical and acoustic transparency, the exposed brain was covered with a 2.5 × 2.5 mm square piece of poly(4-methyl-1-pentene) (PMP) (Goodfellow Cambridge Ltd, Huntingdon, England) (Koekkoek et al., 2018). The gap between the outer edge of the PMP window and the inner edge of the craniotomy was filled with colorless surgical silicone adhesive (Kwik-Sil, World Precision Instruments, Florida), and the PMP window was sealed to the skull with instant adhesive gel (Loctite 454, HenKel, Wisconsin). The metal headbar and exposed skull were covered with dental cement (C&B Metabond, Parkell, New York). Animals were allowed to recover for four days before imaging and sonication experiments.

Optical coherence tomography angiography (OCT-A) system and data acquisition

We built a customized Spectral Domain OCT (SD-OCT) shown in Fig. 1A as our OCT-A device. The system incorporates a superluminescent diode light source (Superlum, cBLMD-T-850-HP, $\lambda_c = 850nm$, $\Delta\lambda = 160nm$) and a spectrometer (Cobra-S 800, Wasatch Photonics) with a line-scan camera (Teledyne e2v) operating at 80 kHz. A 5X objective lens (M Plan Apo NIR, Mitutoyo) with a long working distance was installed in the sample arm. The system's axial and lateral resolution are ~2.5 μm and ~3.5 μm in tissue, respectively.

Custom OCT-system software written in C++ and CUDA was developed to control hardware, including laser control, galvanometers for scanning, and cameras for image acquisition. The OCT images were acquired and processed in near real-time with GPU processing on a high-performance graphic card (GeForce RTX 3090, NVIDIA). A CUDA-based accelerated DFT registration and Split Spectrum Amplitude Decorrelation algorithm (Jia et al., 2012) developed to produce OCT-A images. Angiography processing separated the static reflectance signal from the higher dynamic OCT signal that arises from flowing blood, resulting in relative blood flow images. Each 3D OCT

anatomical volumetric snapshot contained 600 x 600 cross-sectional planes (A-scans × B-scans). repeated frames per B-scans over the same location were acquired for OCT-A. The total acquisition and GPU processing time for each angiographic volume was 30s. En face projections were generated from flattened OCT-A images using MATLAB (MathWorks, Natick, MA).

In situ sonication

To permit simultaneous FUS application and OCT-A angiographic portraits of blood flow, we used a custom mount that permitted fine, 3-axis positioning for a wide-aperture FUS ring transducer (customized H-205B, Sonic Concepts, Inc., Bothell, WA), described in (Fisher and Gumenchuk, 2018). The FUS transducer's fundamental frequency was 510 kHz and achieved a focal spot of lateral width ~3.3 mm (full width at half-maximum) which effectively over-filled the field of view. For the OCT-A modality, the FUS transducer was integrated into the beam path ~2 cm below the primary objective lens. Animals were positioned on a platform atop a lab jack for coarse adjustments (Thorlabs, Inc., NJ). Stimulus waveforms were generated and amplified by a TPO-106 transducer drive system (Sonic Concepts, Inc., Bothell, WA). Sonication was delivered as a 20 s burst 510 kHz ultrasound delivered as a series of 0.5 ms pulses at a repetition rate of 1 kHz (i.e. 50% duty cycle). Two intensities were used, a low of 1 W/cm^2 and a high of 10W/cm^2 (both I_{sppa}). This yielded peak pressures of 0.124 MPa and 0.45 MPa, respectively. Beam properties were characterized in a tank of de-gassed water using a RESON spherically directional hydrophone.

To confirm the colocalized acoustic and optical foci, we used a thermochromic liquid-crystalline sheet (peak thermochromic range 30-35°C) to visualize the FUS focus centroid. Because the OCT illumination center wavelength was near-infrared, the scanned beam OCT beam could be resolved as a "crosshairs" on the thermochromic sheet to correct for any mismatch in position relative to the FUS focus.

Image processing and analysis methods

Image stacks were first processed to remove background noise and co-register to account for any positioning drift between repeated scans. We utilized Top-hat filtering (window width of 6.7 μm) to segment blood vessels and bin by diameter, then applied functions from the Vessel Analysis plugin in ImageJ(Fiji) (Elfarnawany, 2015) for arterioles (15 – 20 μm diameter) for binarization and skeletonization. Capillary-scale (<15 μm diameter) vessel analysis utilized additional functions from VasoMetrics (McDowell et al., 2021).

Experimental data were included in analysis if the animal survived and maintained a stable plane of anesthesia and physiological state during full course of the recording session, which typically lasted 40 minutes from induction to completion. In all, 12 animals were included in our data analysis. Significance was performed in GraphPad Prism-10 (GraphPad Software, CA, USA) and tested using a paired two-tailed Student's t-test with a significant criterion of $\alpha = 0.05$. Normality of the data distribution for any group average was tested using a Shapiro-Wilk test prior to significance analysis.

Immunohistological procedures

Brains were dissected out and postfixed in 4% paraformaldehyde for 24h at 4 °C, after which they were washed in phosphate buffered saline solution (PBS) for one hour then equilibrated in 30% sucrose. Brains were then embedded in OCT compound (Tissue-Tek, Sakura Finetechnical Co., Tokyo, Japan) and sectioned into 18 μm thick coronal sections on a cryotome. Sections were washed and blocked by incubation with 10% normal goat serum (NGS) in PBS supplemented with 0.4% Triton X-100 for 1h at room temperature. They were then incubated with CD31 Rat Monoclonal Antibody (PECAM-1) (1:500 dilution, Abcam 56299) in 2% NGS and 0.3% Triton

X-100 at 4°C overnight. Sections were then incubated for an hour with Alexa-488 labeled secondary antibody (1:500 dilution, goat anti-rat, Abcam150165), after which sections were mounted on slides, dehydrated, and coverslipped with non-fluorescent mounting medium (Krystalon, 64969-95, EMD, Darmstadt, Germany).

Blood-brain barrier disruption was visualized based on the leakage of intraperitoneally administered Evans blue dye into the brain's parenchyma. Half an hour prior to FUS treatment, 0.1mL of a 1% solution of Evans blue dye was injected intraperitoneally. FUS was administered as described above for assessing changes in CD31 distribution. The brain was then dissected out and post-fixed, then prepared as described above for CD31 analysis.

Distribution of Evans blue dye and CD31 was observed using fluorescence imaging with an All-in-One Fluorescence Microscope (Keyence, BZ-X810, Osaka, Japan). The illumination and emission filter parameters for observing Evans blue were 560 ± 28 nm (excitation) and 645 ± 38 nm (emission); for CD31, filter parameters were 470 ± 40 nm excitation, 525 ± 50 nm emission).

Data and Code Availability

The data that support the findings of this study as well as the code used for analysis are available on request from the corresponding author, J.A.N.F.

Competing Interests

The authors declare no competing interests.

Author Contributions

Y.S. performed experiments, analyzed data, and prepared the manuscript, J.V.J. performed data analysis, J.H. performed experiments, M.A., C.R., S.H., and C.Z. engineered the experimental apparatus and contributed to preparing the manuscript, J.A.N.F. performed experiments, performed data analysis, and prepared the manuscript.

Acknowledgements

The authors would like to acknowledge Furong Hu for assistance with immunohistological analysis, tissue preparation and related imaging, Aparna Singh and Elisa Konofagou for assistance calibrating ultrasound systems, and CheukHimIan Lam for assistance with image processing. This work was supported by award R01EB028319 from the National Institute for Biomedical Imaging and Bioengineering to J.A.N.F. as well as R01EB025209, R01HL156265 and R21EB03268401A1 to C.Z.

References

Ai L, Bansal P, Mueller JK, Legon W (2018) Effects of transcranial focused ultrasound on human primary motor cortex using 7T fMRI: a pilot study. BMC Neurosci. 19:56.

Ai L, Bansal P, Mueller JK, Legon W (2018) Effects of transcranial focused ultrasound on human primary motor cortex using 7T fMRI: a pilot study. BMC Neurosci 19:56.

Aumann S, Donner S, Fischer J, Müller F (2019) Optical Coherence Tomography (OCT): Principle and Technical Realization. In: High Resolution Imaging in Microscopy and Ophthalmology: New Frontiers in Biomedical Optics (Bille JF, ed), pp 59–85. Cham: Springer International Publishing.

Blackmore DG, Turpin F, Palliyaguru T, Evans HT, Chicoteau A, Lee W, Pelekanos M, Nguyen N, Song J, Sullivan RKP, Sah P, Bartlett PF, Götz J (2021) Low-intensity ultrasound

restores long-term potentiation and memory in senescent mice through pleiotropic mechanisms including NMDAR signaling. Mol Psychiatry 26:6975–6991.

Blinder P, Tsai PS, Kaufhold JP, Knutsen PM, Suhl H, Kleinfeld D (2013) The cortical angiome: an interconnected vascular network with noncolumnar patterns of blood flow. Nat Neurosci 16:889–897.

Bliss TVP, Collingridge GL (1993) A synaptic model of memory: long-term potentiation in the hippocampus. Nature 361:31–39.

Brown EN, Pavone KJ, Naranjo M (2018) Multimodal General Anesthesia: Theory and Practice. Anesth Analg 127:1246–1258.

Chen S, Nazeri A, Baek H, Ye D, Yang Y, Yuan J, Rubin JB, Chen H (2022) A review of bioeffects induced by focused ultrasound combined with microbubbles on the neurovascular unit. J Cereb Blood Flow Metab 42:3–26.

Ching S, Brown EN (2014) Modeling the dynamical effects of anesthesia on brain circuits. Curr Opin Neurobiol 25:116–122.

Cho EE, Drazic J, Ganguly M, Stefanovic B, Hynynen K (2011) Two-Photon Fluorescence Microscopy Study of Cerebrovascular Dynamics in Ultrasound-Induced Blood—Brain Barrier Opening. J Cereb Blood Flow Metab 31:1852–1862.

Clennell B, Steward TGJ, Elley M, Shin E, Weston M, Drinkwater BW, Whitcomb DJ (2021) Transient ultrasound stimulation has lasting effects on neuronal excitability. Brain Stimul Basic Transl Clin Res Neuromodulation 14:217–225.

Clennell B, Steward TGJ, Hanman K, Needham T, Benachour J, Jepson M, Elley M, Halford N, Heesom K, Shin E, Molnár E, Drinkwater BW, Whitcomb DJ (2023) Ultrasound modulates neuronal potassium currents via ionotropic glutamate receptors. Brain Stimul Basic Transl Clin Res Neuromodulation 16:540–552.

Contreras D, Destexhe A, Sejnowski TJ, Steriade M (1997) Spatiotemporal Patterns of Spindle Oscillations in Cortex and Thalamus. J Neurosci 17:1179–1196.

Dallapiazza RF, Timbie KF, Holmberg S, Gatesman J, Lopes MB, Price RJ, Miller GW, Elias WJ (2018) Noninvasive neuromodulation and brain mapping with low intensity focused ultrasound. J Neurosurg 128:875–884.

Darmani G, Bergmann TO, Butts Pauly K, Caskey CF, de Lecea L, Fomenko A, Fouragnan E, Legon W, Murphy KR, Nandi T, Phipps MA, Pinton G, Ramezanpour H, Sallet J, Yaakub SN, Yoo SS, Chen R (2022) Non-invasive transcranial ultrasound stimulation for neuromodulation. Clin Neurophysiol 135:51–73.

Deffieux T, Younan Y, Wattiez N, Tanter M, Pouget P, Aubry J-F (2013) Low-Intensity Focused Ultrasound Modulates Monkey Visuomotor Behavior. Curr Biol 23:2430–2433.

Deng Z-D, Lisanby SH, Peterchev AV (2013) Electric field depth–focality tradeoff in transcranial magnetic stimulation: simulation comparison of 50 coil designs. Brain Stimulat 6:1–13.

Dudek SM, Bear MF (1992) Homosynaptic long-term depression in area CA1 of hippocampus and effects of N-methyl-D-aspartate receptor blockade. Proc Natl Acad Sci 89:4363–4367.

Earley S, Brayden JE (2015) Transient Receptor Potential Channels in the Vasculature. Physiol Rev 95:645–690.

Elfarnawany MHE-K (2015) Signal processing methods for quantitative power doppler microvascular angiography. The University of Western Ontario (Canada), 2015.

Feldman DE (2009) Synaptic Mechanisms for Plasticity in Neocortex. Annu Rev Neurosci 32:33–55.

Ferrari M, Quaresima V (2012) A brief review on the history of human functional near-infrared spectroscopy (fNIRS) development and fields of application. NeuroImage 63:921–935.

Fisher JAN, Gumenchuk I (2018) Low-intensity focused ultrasound alters the latency and spatial patterns of sensory-evoked cortical responses in vivo. J Neural Eng 15:035004.

Folloni D, Verhagen L, Mars RB, Fouragnan E, Constans C, Aubry J-F, Rushworth MFS, Sallet J (2019) Manipulation of Subcortical and Deep Cortical Activity in the Primate Brain Using Transcranial Focused Ultrasound Stimulation. Neuron 101:1109-1116.e5.

Gili T, Saxena N, Diukova A, Murphy K, Hall JE, Wise RG (2013) The Thalamus and Brainstem Act As Key Hubs in Alterations of Human Brain Network Connectivity Induced by Mild Propofol Sedation. J Neurosci 33:4024–4031.

Griffin MD, Torres VE, Grande JP, Kumar R (1997) Vascular expression of polycystin. J Am Soc Nephrol 8:616.

Guldenmund P, Demertzi A, Boveroux P, Boly M, Vanhaudenhuyse A, Bruno M-A, Gosseries O, Noirhomme Q, Brichant J-F, Bonhomme V, Laureys S, Soddu A (2013) Thalamus, Brainstem and Salience Network Connectivity Changes During Propofol-Induced Sedation and Unconsciousness. Brain Connect 3:273–285.

Hall CN, Reynell C, Gesslein B, Hamilton NB, Mishra A, Sutherland BA, O'Farrell FM, Buchan AM, Lauritzen M, Attwell D (2014) Capillary pericytes regulate cerebral blood flow in health and disease. Nature 508:55–60.

Hameroff S, Trakas M, Duffield C, Annabi E, Gerace MB, Boyle P, Lucas A, Amos Q, Buadu A, Badal JJ (2013) Transcranial Ultrasound (TUS) Effects on Mental States: A Pilot Study. Brain Stimulat 6:409–415.

Harraz OF, Klug NR, Senatore A, Koide M, Nelson MT (2021) Piezo1 is a mechanosensor channel in CNS capillaries: Calcium Signaling and Excitation–Contraction in Cardiac, Skeletal and Smooth Muscle. J Gen Physiol 154:e2021ecc12.

He J, Zhu Y, Wu C, Wu J, Chen Y, Yuan M, Cheng Z, Zeng L, Ji X (2023) Transcranial ultrasound neuromodulation facilitates isoflurane-induced general anesthesia recovery and improves cognition in mice. Ultrasonics 135:107132.

Huang S-L, Chang C-W, Lee Y-H, Yang F-Y (2017) Protective Effect of Low-Intensity Pulsed Ultrasound on Memory Impairment and Brain Damage in a Rat Model of Vascular Dementia. Radiology 282:113–122.

Iacono MI, Neufeld E, Akinnagbe E, Bower K, Wolf J, Oikonomidis IV, Sharma D, Lloyd B, Wilm BJ, Wyss M, Pruessmann KP, Jakab A, Makris N, Cohen ED, Kuster N, Kainz W, Angelone LM (2015) MIDA: A Multimodal Imaging-Based Detailed Anatomical Model of the Human Head and Neck. PLOS ONE 10:e0124126.

Iadecola C (2017) The Neurovascular Unit Coming of Age: A Journey through Neurovascular Coupling in Health and Disease. Neuron 96:17–42.

Jang JH, Solarana K, Hammer DX, Fisher JAN (2021) Dissecting the microvascular contributions to diffuse correlation spectroscopy measurements of cerebral hemodynamics using optical coherence tomography angiography. Neurophotonics 8:025006.

Jia Y, Tan O, Tokayer J, Potsaid B, Wang Y, Liu JJ, Kraus MF, Subhash H, Fujimoto JG, Hornegger J, Huang D (2012) Split-spectrum amplitude-decorrelation angiography with optical coherence tomography. Opt Express 20:4710–4725.

Kim B, Wang T, Li Q, Nam J, Hwang S, Chung E, Kim S, Kim KH (2013) Combined two-photon microscopy and angiographic optical coherence tomography. J Biomed Opt 18:080502.

Kim E, Anguluan E, Youn S, Kim J, Hwang JY, Kim JG (2019) Non-invasive measurement of hemodynamic change during 8 MHz transcranial focused ultrasound stimulation using near-infrared spectroscopy. BMC Neurosci 20:12.

Kim H, Chiu A, Lee SD, Fischer K, Yoo S-S (2014) Focused Ultrasound-mediated Non-invasive Brain Stimulation: Examination of Sonication Parameters. Brain Stimulat 7:748–756.

Kim H-C, Lee W, Weisholtz DS, Yoo S-S (2023) Transcranial focused ultrasound stimulation of cortical and thalamic somatosensory areas in human. PLOS ONE 18:e0288654.

King RL, Brown JR, Newsome WT, Pauly KB (2013) Effective Parameters for Ultrasound-Induced In Vivo Neurostimulation. Ultrasound Med Biol 39:312–331.

Kosnoff J, Yu K, Liu C, He B (2023) Transcranial Focused Ultrasound to V5 Enhances Human Visual Motion Brain-Computer Interface by Modulating Feature-Based

Attention. :2023.09.04.556252 Available at: https://www.biorxiv.org/content/10.1101/2023.09.04.556252v1 [Accessed January 5, 2024].

Kubanek J (2018) Neuromodulation with transcranial focused ultrasound. Neurosurg Focus 44:E14.

Lee KS, Clennell B, Steward TGJ, Gialeli A, Cordero-Llana O, Whitcomb DJ (2022) Focused Ultrasound Stimulation as a Neuromodulatory Tool for Parkinson's Disease: A Scoping Review. Brain Sci 12:289.

Lee W, Chung YA, Jung Y, Song I-U, Yoo S-S (2016) Simultaneous acoustic stimulation of human primary and secondary somatosensory cortices using transcranial focused ultrasound. BMC Neurosci 17:68.

Lee W, Kim H, Jung Y, Song I-U, Chung YA, Yoo S-S (2015) Image-Guided Transcranial Focused Ultrasound Stimulates Human Primary Somatosensory Cortex. Sci Rep 5

Lee W, Kim S, Kim B, Lee C, Chung YA, Kim L, Yoo S-S (2017) Non-invasive transmission of sensorimotor information in humans using an EEG/focused ultrasound brain-to-brain interface. PLOS ONE 12:e0178476.

Legon W, Bansal P, Tyshynsky R, Ai L, Mueller JK (2018) Transcranial focused ultrasound neuromodulation of the human primary motor cortex. Sci Rep 8:10007.

Legon W, Sato TF, Opitz A, Mueller J, Barbour A, Williams A, Tyler WJ (2014) Transcranial focused ultrasound modulates the activity of primary somatosensory cortex in humans. Nat Neurosci 17:322–329.

Leinenga G, Götz J (2015) Scanning ultrasound removes amyloid-β and restores memory in an Alzheimer's disease mouse model. Sci Transl Med 7:278ra33-278ra33.

Lin W-T, Chen R-C, Lu W-W, Liu S-H, Yang F-Y (2015) Protective effects of low-intensity pulsed ultrasound on aluminum-induced cerebral damage in Alzheimer's disease rat model. Sci Rep 5:9671.

Llinás RR, Steriade M (2006) Bursting of Thalamic Neurons and States of Vigilance. J Neurophysiol 95:3297–3308.

Lu G, Qian X, Castillo J, Li R, Jiang L, Lu H, Kirk Shung K, Humayun MS, Thomas BB, Zhou Q (2021) Transcranial Focused Ultrasound for Noninvasive Neuromodulation of the Visual Cortex. IEEE Trans Ultrason Ferroelectr Freq Control 68:21–28.

Ma X, Cheng K-T, Wong C-O, O'Neil RG, Birnbaumer L, Ambudkar IS, Yao X (2011) Heteromeric TRPV4-C1 channels contribute to store-operated Ca2+ entry in vascular endothelial cells. Cell Calcium 50:502–509.

Mashour GA, Alkire MT (2013) Consciousness, Anesthesia, and the Thalamocortical System. Anesthesiology 118:13–15.

McDannold N, Maier SE (2008) Magnetic resonance acoustic radiation force imaging. Med Phys 35:3748–3758.

McDowell KP, Berthiaume A-A, Tieu T, Hartmann DA, Shih AY (2021) VasoMetrics: unbiased spatiotemporal analysis of microvascular diameter in multi-photon imaging applications. Quant Imaging Med Surg 11:969–982.

Narayanan D, Bulley S, Leo MD, Burris SK, Gabrick KS, Boop FA, Jaggar JH (2013) Smooth muscle cell transient receptor potential polycystin-2 (TRPP2) channels contribute to the myogenic response in cerebral arteries. J Physiol 591:5031–5046.

Neuling T, Wagner S, Wolters C, Zaehle T, Herrmann C (2012) Finite-Element Model Predicts Current Density Distribution for Clinical Applications of tDCS and tACS. Front Psychiatry 3

Newman M, Rasiah PK, Kusunose J, Rex TS, Mahadevan-Jansen A, Hardenburger J, Jansen ED, Millis B, Caskey CF (2023) Ultrasound Modulates Calcium Activity in Cultured Neurons, Glial Cells, Endothelial Cells and Pericytes. Ultrasound Med Biol

Niu X, Yu K, He B (2022) Transcranial focused ultrasound induces sustained synaptic plasticity in rat hippocampus. Brain Stimulat 15:352–359.

Oh S-J, Lee JM, Kim H-B, Lee J, Han S, Bae JY, Hong G-S, Koh W, Kwon J, Hwang E-S, Woo DH, Youn I, Cho I-J, Bae YC, Lee S, Shim JW, Park J-H, Lee CJ (2019) Ultrasonic Neuromodulation via Astrocytic TRPA1. Curr Biol CB 29:3386-3401.e8.

Phillips AA, Chan FH, Zheng MMZ, Krassioukov AV, Ainslie PN (2016) Neurovascular coupling in humans: Physiology, methodological advances and clinical implications. J Cereb Blood Flow Metab 36:647–664.

Plaksin M, Kimmel E, Shoham S (2016) Cell-Type-Selective Effects of Intramembrane Cavitation as a Unifying Theoretical Framework for Ultrasonic Neuromodulation. eNeuro 3:ENEURO.0136-15.2016.

Pober JS, Cotran RS (1990) THE ROLE OF ENDOTHELIAL CELLS IN INFLAMMATION. Transplantation 50:537.

Rampersad SM, Janssen AM, Lucka F, Aydin Ü, Lanfer B, Lew S, Wolters CH, Stegeman DF, Oostendorp TF (2014) Simulating Transcranial Direct Current Stimulation With a Detailed Anisotropic Human Head Model. IEEE Trans Neural Syst Rehabil Eng 22:441–452.

Ranade SS, Qiu Z, Woo S-H, Hur SS, Murthy SE, Cahalan SM, Xu J, Mathur J, Bandell M, Coste B, Li Y-SJ, Chien S, Patapoutian A (2014) Piezo1, a mechanically activated ion

channel, is required for vascular development in mice. Proc Natl Acad Sci 111:10347–10352.

Raymond SB, Skoch J, Hynynen K, Bacskai BJ (2007) Multiphoton imaging of ultrasound/Optison mediated cerebrovascular effects in vivo. J Cereb Blood Flow 38 Metab 27:393–403.

Redinbaugh MJ, Phillips JM, Kambi NA, Mohanta S, Andryk S, Dooley GL, Afrasiabi M, Raz A, Saalmann YB (2020) Thalamus Modulates Consciousness via Layer-Specific Control of Cortex. Neuron 106:66-75.e12.

Retailleau K, Duprat F, Arhatte M, Ranade SS, Peyronnet R, Martins JR, Jodar M, Moro C, Offermanns S, Feng Y, Demolombe S, Patel A, Honoré E (2015) Piezo1 in Smooth Muscle Cells Is Involved in Hypertension-Dependent Arterial Remodeling. Cell Rep 13:1161–1171.

Rohani M, Fasano A (2017) Focused Ultrasound for Essential Tremor: Review of the Evidence and Discussion of Current Hurdles. Tremor Hyperkinetic Mov 7:462.

Saturnino GB, Madsen KH, Thielscher A (2019) Electric field simulations for transcranial brain stimulation using FEM: an efficient implementation and error analysis. J Neural Eng 16:066032.

Sharabi S, Daniels D, Last D, Guez D, Zivli Z, Castel D, Levy Y, Volovick A, Grinfeld J, Rachmilevich I, Amar T, Mardor Y, Harnof S (2019) Non-thermal focused ultrasound induced reversible reduction of essential tremor in a rat model. Brain Stimulat 12:1–8.

Shin DW, Fan J, Luu E, Khalid W, Xia Y, Khadka N, Bikson M, Fu BM (2020) In vivo modulation of the blood-brain barrier permeability by transcranial direct current stimulation (tDCS). Ann Biomed Eng 48:1256–1270.

Slupe AM, Kirsch JR (2018) Effects of anesthesia on cerebral blood flow, metabolism, and neuroprotection. J Cereb Blood Flow Metab 38:2192–2208.

Strangman G, Boas DA, Sutton JP (2002a) Non-invasive neuroimaging using near-infrared light. Biol Psychiatry 52:679–693.

Strangman G, Culver JP, Thompson JH, Boas DA (2002b) A Quantitative Comparison of Simultaneous BOLD fMRI and NIRS Recordings during Functional Brain Activation. NeuroImage 17:719–731.

Sweeney PW, Walker-Samuel S, Shipley RJ (2018) Insights into cerebral haemodynamics and oxygenation utilising in vivo mural cell imaging and mathematical modelling. Sci Rep 8:1373.

Tiruppathi C, Ahmmed GU, Vogel SM, Malik AB (2006) Ca2+ Signaling, TRP Channels, and Endothelial Permeability. Microcirculation 13:693–708.

Todd N, Zhang Y, Livingstone M, Borsook D, McDannold N (2019) The neurovascular response is attenuated by focused ultrasound-mediated disruption of the blood-brain barrier. NeuroImage 201:116010.

Torres VE, Cai Y, Chen X, Wu GQ, Geng L, Cleghorn KA, Johnson CM, Somlo S (2001) Vascular Expression of Polycystin-2. J Am Soc Nephrol 12:1.

Tufail Y, Yoshihiro A, Pati S, Li MM, Tyler WJ (2011) Ultrasonic neuromodulation by brain stimulation with transcranial ultrasound. Nat Protoc 6:1453–1470.

White NS, Alkire MT (2003) Impaired thalamocortical connectivity in humans during general-anesthetic-induced unconsciousness. NeuroImage 19:402–411.

Yoo S, Mittelstein DR, Hurt RC, Lacroix J, Shapiro MG (2022) Focused ultrasound excites cortical neurons via mechanosensitive calcium accumulation and ion channel amplification. Nat Commun 13:493.

Yoo S-S, Bystritsky A, Lee J-H, Zhang Y, Fischer K, Min B-K, McDannold NJ, Pascual-Leone A, Jolesz FA (2011a) Focused ultrasound modulates region-specific brain activity. Neuroimage 56:1267–1275.

Yoo S-S, Kim H, Filandrianos E, Taghados SJ, Park S (2013) Non-Invasive Brain-to-Brain Interface (BBI): Establishing Functional Links between Two Brains. PLOS ONE 8:e60410.

Yoo S-S, Kim H, Min B-K, Eric Franck SP (2011b) Transcranial Focused Ultrasound to the Thalamus Alters Anesthesia Time in Rats. Neuroreport 22:783–787.

Yoo S-S, Yoon K, Croce P, Cammalleri A, Margolin RW, Lee W (2018) Focused ultrasound brain stimulation to anesthetized rats induces long-term changes in somatosensory evoked potentials. Int J Imaging Syst Technol 28:106–112.

Yuan Y, Wang Z, Liu M, Shoham S (2020) Cortical hemodynamic responses induced by low-intensity transcranial ultrasound stimulation of mouse cortex. NeuroImage 211:116597.

Yuan Y, Wu Q, Wang X, Liu M, Yan J, Ji H (2023) Low-intensity ultrasound stimulation modulates time-frequency patterns of cerebral blood oxygenation and neurovascular coupling of mouse under peripheral sensory stimulation state. NeuroImage 270:119979.

Yuan Y, Zhao Y, Jia H, Liu M, Hu S, Li Y, Li X (2018) Cortical Hemodynamic Responses Under Focused Ultrasound Stimulation Using Real-Time Laser Speckle Contrast Imaging. Front Neurosci 12

Yüksel MM, Sun S, Latchoumane C, Bloch J, Courtine G, Raffin EE, Hummel FC (2023) Low-Intensity Focused Ultrasound Neuromodulation for Stroke Recovery: A Novel Deep Brain Stimulation Approach for Neurorehabilitation? IEEE Open J Eng Med Biol 4:300–318.

Zhao Z, Ji H, Zhang C, Pei J, Zhang X, Yuan Y (2023) Modulation effects of low-intensity transcranial ultrasound stimulation on the neuronal firing activity and synaptic plasticity of mice. NeuroImage 270:119952.

Zhong Y-X, Liao J-C, Liu X, Tian H, Deng L-R, Long L (2023) Low intensity focused ultrasound: a new prospect for the treatment of Parkinson's disease. Ann Med 55:2251145.

Figure Captions

Figure 1: Combined optical coherence tomography angiography (OCT-A) and FUS for observing multi-scale vascular responses to sonication. **A** depicts a schematic for a custom frequency domain OCT-A apparatus with in-line FUS ring transducer. The inset shows a sample 1 mm × 1 mm *en face* z-projection revealing flow patterns measured in somatosensory cortex. **B** shows a sample 3D surface mesh rendering of vascular architecture, as reconstructed from OCT-A imagery. **C** shows the lateral profile of the FUS beam (scale bar = 1 mm), and **D** illustrates the pulsed sonication protocol; sonication was delivered as a 20 s period of 510 kHz ultrasound pulsed at 1 kHz with 50% duty cycle.

Figure 2: Depth-resolved flow patterns in the somatosensory cortex. **A** and **B** show z-projections from narrow ranges of lateral slices centered at the most superficial 200 μm of the cortex and ~510 μm. The depth range for projections in **A** and **B** is ± ~2 μm axially. **C** depicts a histogram of vessel diameters, among all animals. **D** shows data from all depths, which is here encoded by color. As is apparent, consistent with known cerebrovascular architecture, the deepest features resolve a fine mesh of narrow vessel branches.

Figure 3: Diameter-specific analysis of flow measurements. **A** depicts a z-projection of a 1 mm × 1 mm × 540 μm region of somatosensory cortex *in vivo*. **B** illustrates diameter-specific segmentation of microvascular diameter vessel branches; red vessel branches in **C** were auto-selected for analysis because they could be resolved throughout all conditions. **D** shows an example of large diameter vessel branch segmentation, and **E** illustrates, in a magnified subregion of **D**, the vessel "tagging" feature of our data analysis pipeline, which enabled us to track individual vessel branches through the course of FUS application.

Figure 4: Dissecting vascular effects of FUS *in vivo*. Normalized changes in vessel branch diameters, averaged over all animals, are binned based on pre-FUS diameter ranges: >20 μm (**A**), 15-20 μm (**B**), and <15 μm (**C**). Vessels of pre-FUS diameter less than 15 μm, but not larger vessels, displayed significant increases in diameter that persisted beyond 10 minutes. Values displayed atop brackets in **C** report *P*-values that were below 0.05, obtained using a paired, two-tailed Student's t-test. **D** shows OCT-A monitoring in single vessel branches during the course of consecutive doses of FUS. The yellow square in the left-most image shows a region that is expanded in images to the right. The scale bar in the full image on left is 1 mm × 1 mm, and the scale bar for smaller images on the right is 110 μm × 110 μm. The waveforms between sub-images are cartoon representations of the FUS pulses; sonication consists of pulse bursts that are delivered at a rate of 1 kHz over a period of 20 sec.

Figure 5: Immunohistochemical assessment of vascular integrity and BBB permeabilization. **A** shows an illustration of the relative coordinates on the brain where FUS was targeted. The more medial location received higher intensity sonication (>200 W/cm^2 I_{sppa}, 100% duty cycle, 20 s), while the lateral location was sonicated at a lower intensity (1.2 W/cm^2, 100% duty cycle for 20s). **B-D** show coronal sections obtained at the rostrocaudal axis location where sonication was performed. The magenta and cyan arrows represent, respectively, high- and low-intensity sonication locations. CD31 labeling is displayed in **B**, Evans blue in **C**, and **D** shows a merged image.

Table 1: Analysis results from FUS treatment averaged among all experiments. Values following treatment are reported as normalized diameters. In addition to the changes summed over all vessel branch diameters, analysis is reported for selected diameter ranges. *P*-values were obtained using a paired, two-tailed Student's t-test. Diameter values are reported as mean ± standard deviation.

Figure S1: Diameter changes in response to repeated doses of FUS at (**A**) 1 W/cm^2 and (**B**) 10 W/cm^2. The data represents vessel branches of diameter < 15 μm.

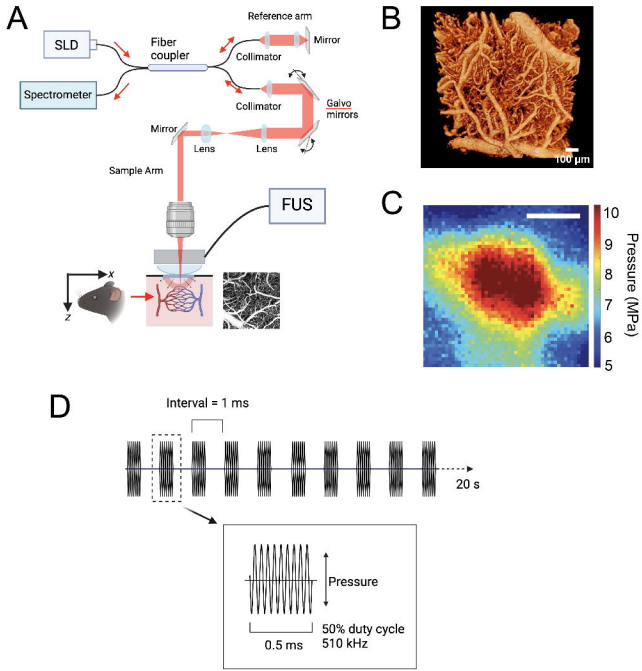
A
SLD
Spectrometer
Fiber coupler
Reference arm
Mirror
Collimator
Collimator
Galvo mirrors
Mirror
Lens
Lens
Sample Arm
FUS
x
z
B
100 µm
C
10
9
8
7
6
5
Pressure (MPa)
D
Interval = 1 ms
20 s
Pressure
0.5 ms
50% duty cycle
510 kHz

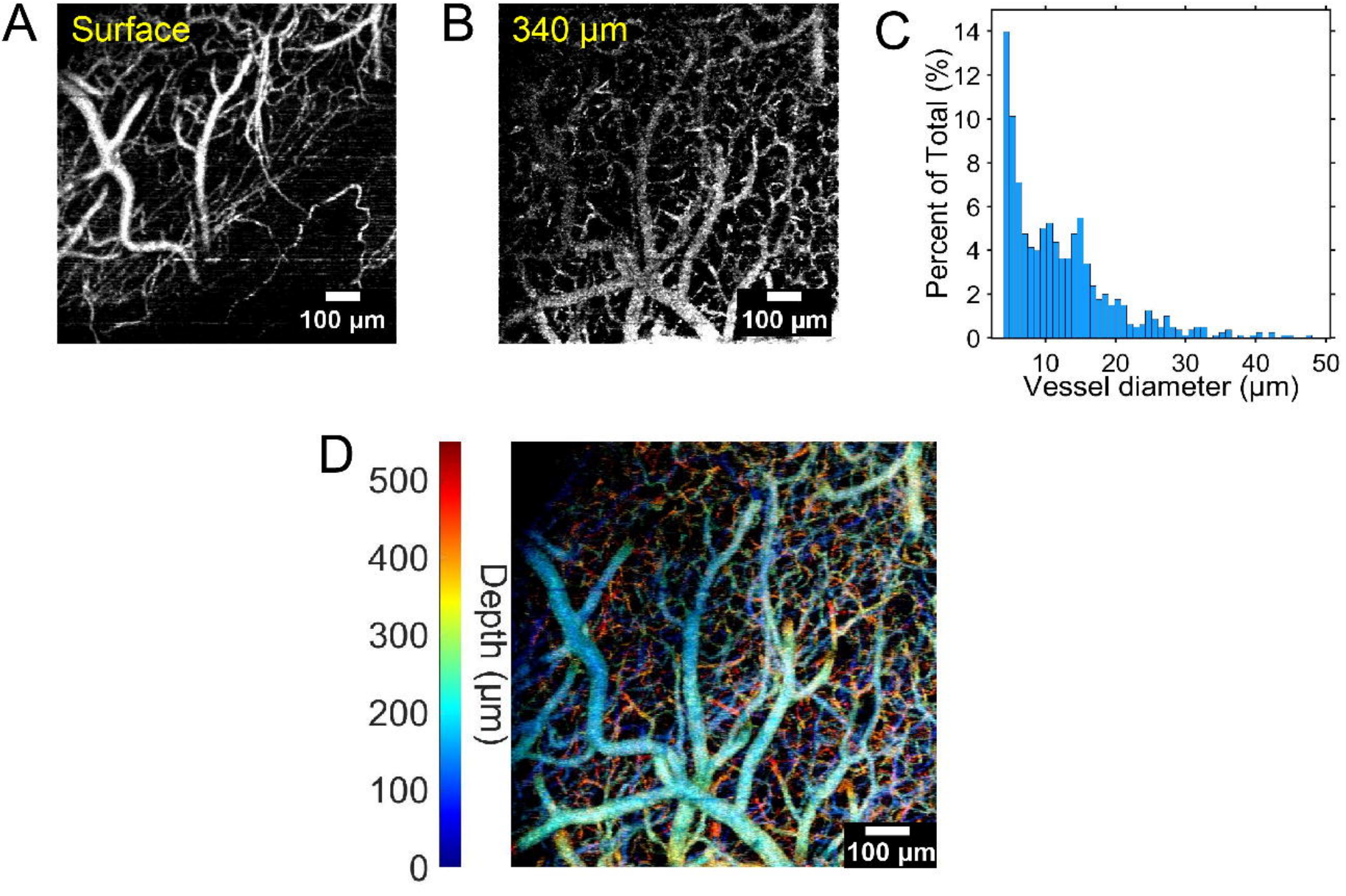
A
Surface
100 µm
B
340 µm
100 µm
C
Percent of Total (%)
0
2
4
6
8
10
12
14
10
20
30
40
50
Vessel diameter (µm)
D
500
400
300
200
100
0
Depth (µm)
100 µm

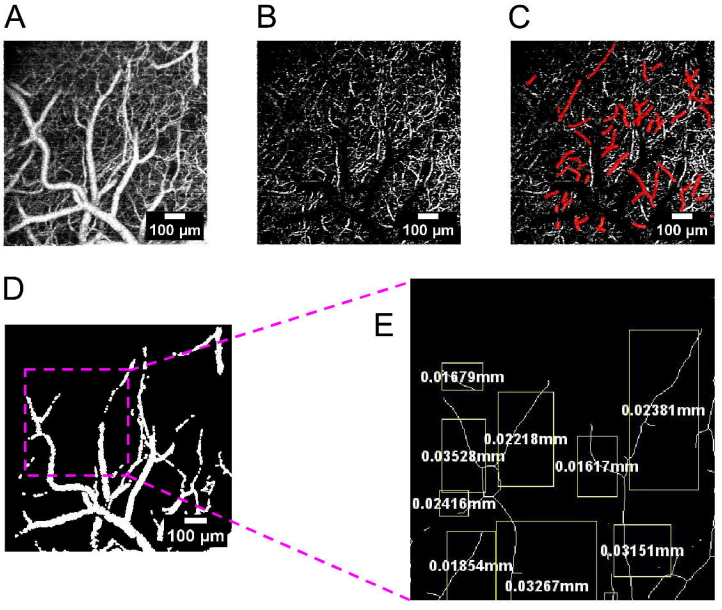
A
100 µm
B
100 µm
C
100 µm
D
100 µm
E
0.01679mm
0.02218mm
0.02381mm
0.03528mm
0.01617mm
0.02416mm
0.01854mm
0.03267mm
0.03151mm

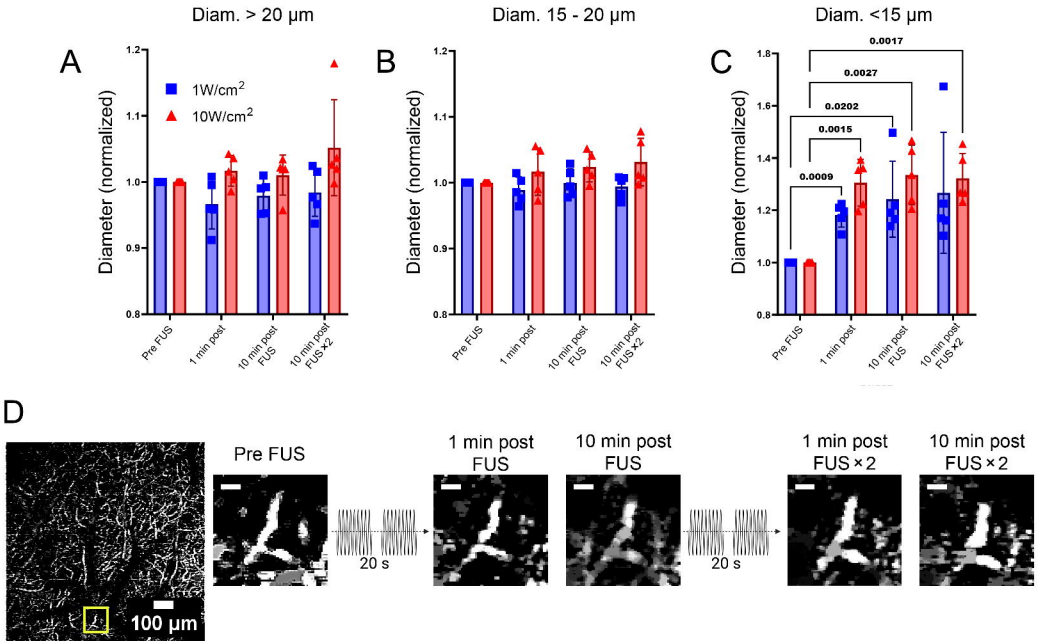
Diam. > 20 µm
Diam. 15 - 20 µm
Diam. <15 µm
A
B
C
1W/cm2
10W/cm2
Diameter (normalized)
1.2
1.1
1.0
0.9
0.8
1.8
1.6
1.4
1.2
0.0017
0.0027
0.0202
0.0015
0.0009
Pre FUS
1 min post
10 min post FUS
10 min post FUS×2
D
100 µm
Pre FUS
1 min post FUS
10 min post FUS
1 min post FUS × 2
10 min post FUS × 2
20 s
20 s

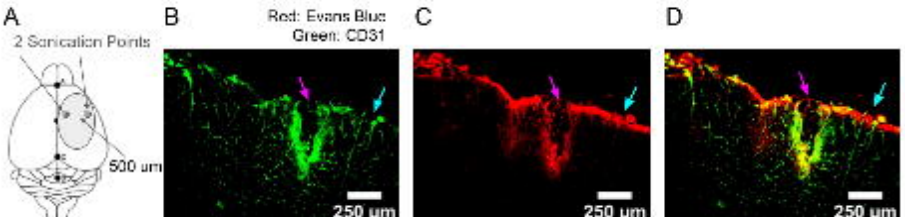
A
2 Sonication Points
500 um
B
Red: Evans Blue
Green: CD31
250 µm
C
250 µm
D
250 µm

Diam. range	FUS intensity (I_{sppa})	Diameter pre-FUS (μm)	Normalized diameter, 1 min post FUS	Normalized diameter, 10 min post FUS	Normalized diameter, 10 min post FUS × 2	*P*-value, comparison with pre-FUS	*P*-value, comparison with response to first FUS dose
All vessels	Control	13.36±14.05	1.01±1.02	1.12±1.12	1.00±1.05	–	–
All vessels	1 W/cm^2	14.01±13.51	1.04±0.09	1.06±0.09	1.05±0.09	0.0094	–
All vessels	10 W/cm^2	19.21±13.95	1.10±0.11	1.11±0.12	1.13±0.12	0.7737	0.0672
> 20 μm	Control	36.45±19.29	1.00±0.53	1.03±0.53	0.97±0.51	–	–
> 20 μm	1 W/cm^2	33.34±16.89	0.97±0.03	0.98±0.02	0.98±0.03	0.1529	–
> 20 μm	10 W/cm^2	31.95±11.61	1.02±0.03	1.01±0.03	1.05±0.06	0.0439	0.0827
15 - 20 μm	Control	16.64±0.98	1.01±0.05	1.00±0.06	1.02±0.04	–	–
15 - 20 μm	1 W/cm^2	17.59±1.40	0.99±0.02	1.00±0.02	1.00±0.02	0.4879	–
15 - 20 μm	10 W/cm^2	17.35±1.38	1.02±0.03	1.02±0.02	1.03±0.03	0.0732	0.0666
< 15 μm	Control	5.94±1.50	1.00±0.30	1.01±0.24	0.99±0.27	–	–
< 15 μm	1 W/cm^2	5.89±1.04	1.18±0.04	1.24±0.13	1.27±0.21	0.0194	–
< 15 μm	10 W/cm^2	6.28±1.30	1.31±0.08	1.33±0.10	1.32±0.09	0.0016	0.0836

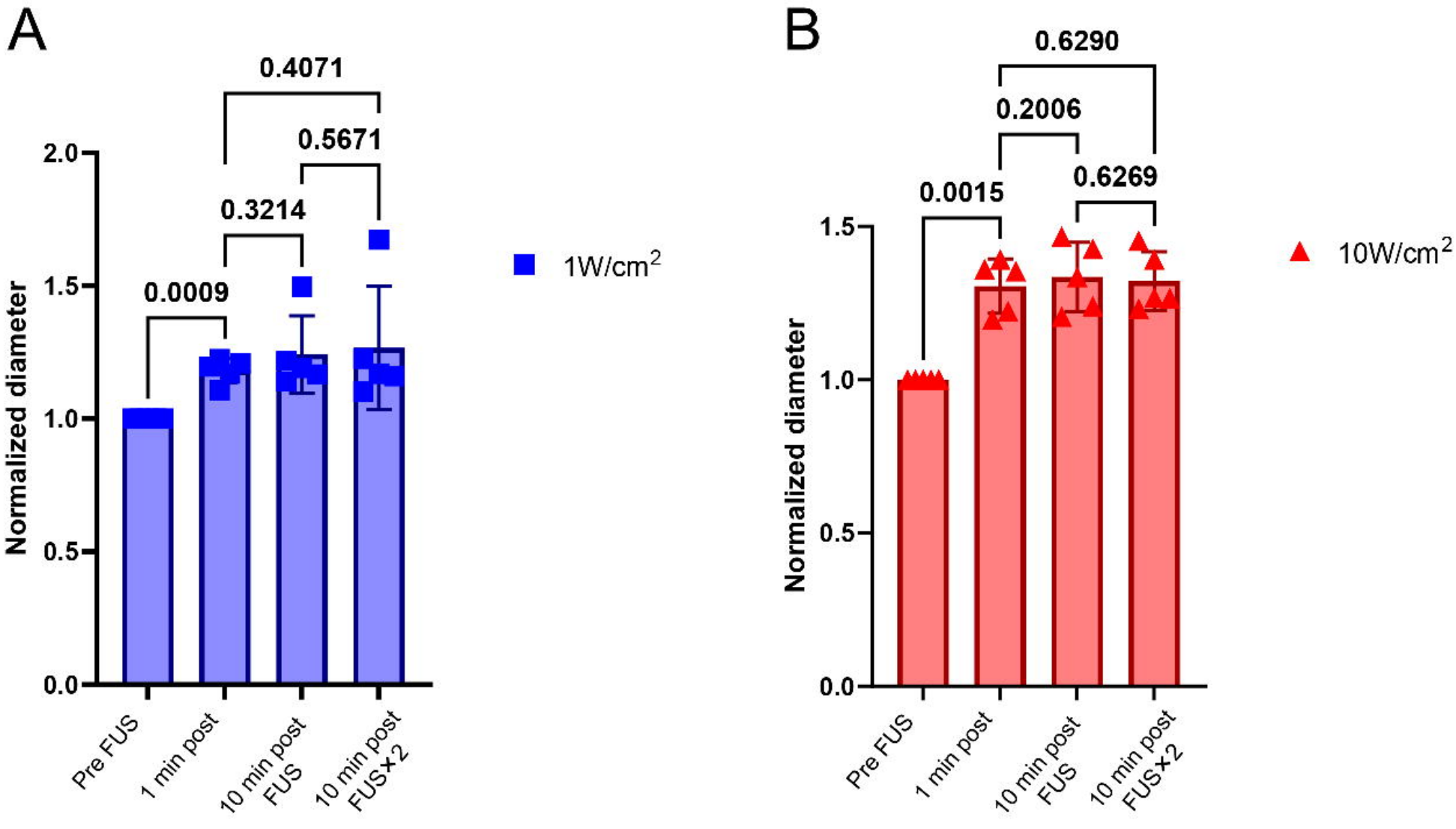
A
0.4071
0.5671
0.3214
0.0009
2.0
1.5
1.0
0.5
0.0
Normalized diameter
Pre FUS
1 min post
10 min post FUS
10 min post FUS×2
1W/cm2
B
0.6290
0.2006
0.6269
0.0015
1.5
1.0
0.5
0.0
Normalized diameter
Pre FUS
1 min post
10 min post FUS
10 min post FUS×2
10W/cm2